

Forecasting Human Dynamics from Static Images

Yu-Wei Chao¹, Jimei Yang², Brian Price², Scott Cohen², and Jia Deng¹

¹University of Michigan, Ann Arbor
{ywchao, jiadeng}@umich.edu

²Adobe Research
{jimyang, bprice, scohen}@adobe.com

Abstract

This paper presents the first study on forecasting human dynamics from static images. The problem is to input a single RGB image and generate a sequence of upcoming human body poses in 3D. To address the problem, we propose the 3D Pose Forecasting Network (3D-PFNet). Our 3D-PFNet integrates recent advances on single-image human pose estimation and sequence prediction, and converts the 2D predictions into 3D space. We train our 3D-PFNet using a three-step training strategy to leverage a diverse source of training data, including image and video based human pose datasets and 3D motion capture (MoCap) data. We demonstrate competitive performance of our 3D-PFNet on 2D pose forecasting and 3D pose recovery through quantitative and qualitative results.

1. Introduction

Human pose forecasting is the capability of predicting future human body dynamics from visual observations. Human beings are endowed with this great ability. For example, by looking at the left image of Fig. 1, we can effortlessly imagine the upcoming body dynamics of the target tennis player, namely a forehand swing, as shown in the right image of Fig. 1. Such prediction is made by reasoning on the scene context (i.e. a tennis court), the current body pose of the target (i.e. standing and holding a tennis racket), and our visual experience of a tennis forehand swing.

The ability of forecasting reflects a higher-level intelligence beyond perception and recognition and plays an important role for agents to survive from challenging natural and social environments. In the context of human-robot interactions, such ability is particularly crucial for assistant robots that need to interact with surrounding humans in an efficient and robust manner. Apparently, the abilities of identifying and localizing the action categories [24, 6, 37, 23] after observing an image or video are not sufficient to achieve this goal. For example, when a person throws a ball at a robot, the robot needs to identify the ac-

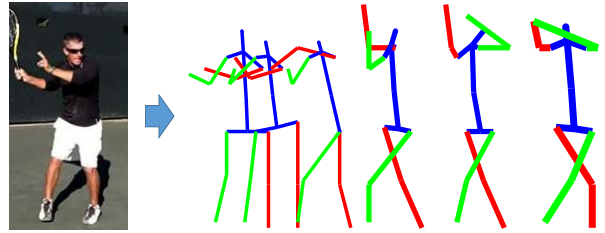


Figure 1: Forecasting human dynamics from static images. Left: the input image. Right: the sequence of upcoming poses.

tion and forecast the body pose trajectory even before the person finishes so that it can respond effectively (either by catching the ball or dodging it).

This paper presents the first study on human pose forecasting from static images. Our task is to take a single RGB image and output a sequence of future human body poses. Our approach has two key features. First, as opposed to other forecasting tasks that assume a multi-frame input (i.e. videos) [25, 9, 17], our work assumes a single-frame input. Although this assumption increases the learning challenge due to the lack of explicit motion cues, it encourages the algorithm to learn high-level dynamics instead of low-level smoothness. Note that our approach can be trivially extended to take multi-frame inputs as shown later in the methodology section. Second, like most forecasting problems [38, 30, 21, 31, 29], we first represent the forecasted poses in the 2D image space. However, we include an extra component to our approach to further convert each forecasted pose from 2D space to 3D space. Both forecasting and 3D conversion are performed using a deep neural network (DNN). The two networks are integrated into one single unified framework to afford end-to-end training. Since human bodies feature a complex articulated structure, we believe the 3D output is more actionable and useful for future applications (e.g. shape and texture rendering) as we demonstrate in the supplementary materials.

The main contributions of this paper are three-fold: (1) We present the first study on single-frame human pose forecasting. This extends the dimension of current studies on human pose modeling from recognition (i.e. pose estima-

tion [27, 19]) to forecasting. The problem of pose forecasting in fact generalizes pose estimation, since to forecast future poses we need to first estimate the observed pose. (2) We propose a novel DNN-based approach to address the problem. Our forecasting network integrates recent advances on single-image human pose estimation and sequence prediction. Experimental results show that our approach outperforms strong baselines on 2D pose forecasting. (3) We propose an extra network to convert the forecasted 2D poses into 3D skeletons. Our 3D recovery network is trained on a vast amount of synthetic examples by leveraging motion capture (MoCap) data. Experimental results show that our approach outperforms two state-of-the-art methods on 3D pose recovery. In a nutshell, we propose a unified framework for 2D pose forecasting and 3D pose recovery. Our *3D Pose Forecasting Network* (3D-PFNet) is trained by leveraging a diverse source of training data, including image and video based human pose datasets and MoCap data. We separately evaluate our 3D-PFNet on 2D pose forecasting and 3D pose recovery, and show competitive results over baselines.

2. Related Work

Visual Scene Forecasting Our work is in line with a series of recent work on single-image visual scene forecasting. These works vary in the predicted target and the output representation. [15] predicts human actions in the form of semantic labels. Some others predict motions of low level image features, such as the optical flow to the next frame [21, 31] or dense trajectories of pixels [38, 29]. A few others attempt to predict the motion trajectories of middle-level image patches [30] or rigid objects [18]. However, these methods do not explicitly output a human body model, thus cannot directly address human pose forecasting. Notably, [9] predicts the future dynamics of a 3D human skeleton from its past motion. Despite its significance, their method can be applied to only 3D skeleton data but not visual inputs. Our work is the first attempt to predict 3D human dynamics from RGB images.

Human Pose Estimation Our work is closely related to the problem of human pose estimation, which has long been attractive in computer vision. Human bodies are commonly represented by tree-structured skeleton models, where each node is a body joint and the edges capture articulation. The goal is to estimate the 2D joint locations in the observed image [27, 19] or video sequences [20, 10]. Recent work has even taken one step further to directly recover 3D joint locations [16, 36, 26, 7, 4, 22] or body shapes [3] from image observations. While promising, these approaches can only estimate the pose of humans in the observed image or video. Our approach not only estimate the human pose in the observed image, but also forecasts the poses in the upcoming

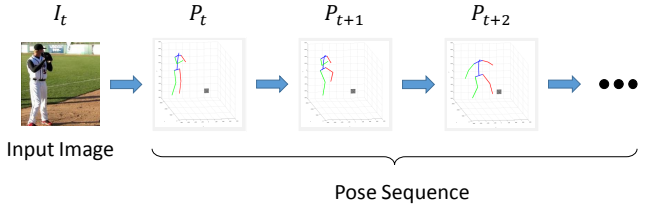


Figure 2: The problem of human pose prediction. The input is a single image, and the output is a 3D pose sequence.

frames. Besides estimation from images or videos, an orthogonal line of research addresses the recovery of 3D body joint locations from their 2D projections [1, 40, 41, 32]. Our work also takes advantage of these approaches to transform the estimated 2D joint locations into 3D space.

Video Frame Synthesis Two very recent works [33, 28] attempt to synthesize videos from static images by predicting pixels in future frames. This is a highly challenging problem due to the extremely high dimensional output space and the massive variations a scene can transform from a single image. Our work can provide critical assistance to this task by using the predicted human poses as intermediate representation to regularize frame synthesis, e.g. it is easier to synthesize a baseball pitching video from a single photo of a player if we can forecast his body dynamics. In addition to static images, there are also other efforts addressing video prediction from video inputs [25, 17, 8], which can be benefited by our work in the same way.

3. Approach

3.1. Problem Statement

The problem studied in this paper assumes the input to be a single image captured at time t . The output is a sequence of 3D human body skeletons $P = \{P_t, \dots, P_{t+T}\}$, where $P_i \in \mathbb{R}^{3 \times N}$ denotes the predicted skeleton at time i , represented by the 3D locations of N keypoints. See Fig. 2 for an illustration of the problem. Note that this formulation generalizes single-frame 3D human pose estimation, which can be viewed as a special case when $T = 0$.

3.2. Network Architecture

We propose a deep recurrent network to predict human skeleton sequences (Fig. 3). The network is divided into two components: first, a 2D pose sequence generator that takes an input image and sequentially generates 2D body poses, where each pose is represented by heatmaps of keypoints; second, a 3D skeleton converter that converts each 2D pose into a 3D skeleton.

2D Pose Sequence Generator The first step is to generate a 2D body pose sequence from the input image. The task can be decomposed into estimating the body pose in

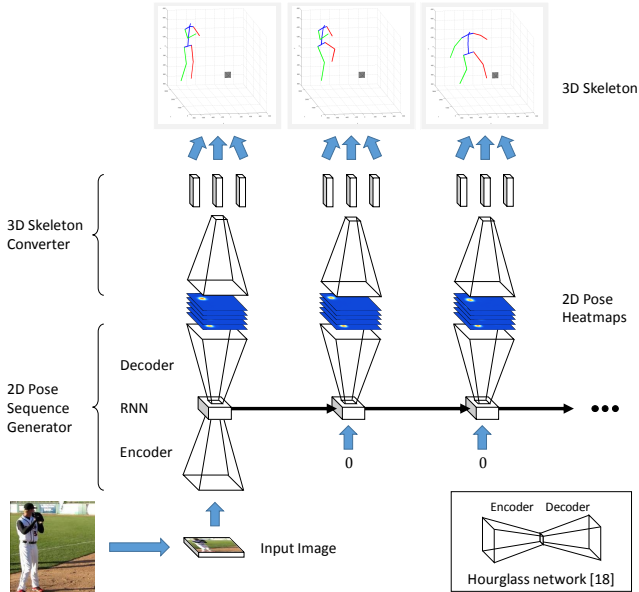


Figure 3: A schematic view of the unrolled 3D-PFNet.

the given frame and predicting the body poses in upcoming frames. We thus leverage recent advances on single-frame human pose estimation as well as sequence prediction. The recently introduced *hourglass* networks [19] have demonstrated state-of-the-art performance on large-scale human pose datasets [2]. We summarize the hourglass architecture as follows: The first half of the hourglass processes the input image with convolution and pooling layers to a set of low resolution feature maps. This resembles conventional ConvNets (and is frequently referred to as “encoder” in generative models). The second half (frequently referred to as “decoder”) then processes the low resolution feature maps with a symmetric set of upsampling and convolution layers to generate dense detection heatmaps for each keypoint at high resolution. A critical issue of this architecture is the loss of high resolution information in the encoder output due to pooling. Thus one key ingredient is to add a “skip connection” before each pooling layer to create a direct path to the counterpart in the decoder. As a result, the hourglass can consolidate features from multiple scales in generating detection outputs.

While achieving promising results on single-frame pose estimation, the hourglass network is incapable of predicting future poses. A straightforward extension is to increase the channel size of its output to jointly generate predictions for future frames [29, 28]. However, the drawback is that a trained network will always predict output for a fixed number of frames. To bypass this constraint, we choose to formulate pose forecasting as a sequence prediction problem by adopting recurrent neural networks (RNNs).

RNNs extend conventional DNNs with feedback loops to enable sequential prediction from internal states driven by

both current and pass observations. Our key idea is to introduce an RNN to the neck of the hourglass, i.e. between the encoder and decoder. We hypothesize that the global pose features encoded in the low resolution feature maps are sufficient to drive the future predictions. We refer to the new network as the *recurrent hourglass* architecture. Fig. 3 illustrates the process of generating pose sequence from the unrolled version of the recurrent hourglass network. First, the given image is passed into the encoder to generate low resolution feature maps. These feature maps are then processed by an RNN to update its internal states. Note that the internal states here can be viewed as the “belief” on the current pose. This “belief” is then passed to the decoder to generate pose heatmaps for the input image. To generate pose for the next timestep, this “belief” is fed back to the RNN and then updated to account for the pose change. The updated “belief” is again passed to the decoder to generate heatmaps for the second timestep. This process will repeat, and in the end we will obtain a sequence of 2D pose heatmaps. Since we assume a single-image input, the encoder is used only in the initial frame. Starting from the second frame, the input to RNN is set to zeros. As mentioned earlier, it is natural to extend our model to video inputs by adding an encoder at every timestep.

For the RNN, we adopt the long short-term memory (LSTM) architecture [14] due to its strength in preserving long-term memory. We apply two tricks: First, conventional LSTMs are used in fully-connected architectures. Since the hourglass network is fully convolutional and the encoder output is a feature map, we apply the LSTM convolutionally on each pixel. This is equivalent to replacing the fully-connected layers in LSTM by 1×1 convolution layers. Second, we apply the residual architecture [11] in our RNN to retain a direct path from the encoder to the decoder. As a result, we place less burden on the RNN as it only needs to learn the “changes” in poses. Fig. 4 (a) shows the detailed architecture of our recurrent hourglass networks. Note that we also place an RNN on the path of each skip connection of the hourglass.

3D Skeleton Converter The second step is to convert the heatmap sequence into a sequence of 3D skeletons. Many recent works have addressed the problem of recovering 3D skeleton structures from the 2D projection of their keypoints [40, 32]. Zhou *et al.* [40] assumes the unknown 3D pose can be approximated by a linear combination of a set of predefined basis poses, and propose to minimize reprojection error with a convex relaxation approach. Wu *et al.* [32] adopts a similar assumption but instead uses a DNN to estimate the linear coefficients and camera parameters. Both methods use a top-down approach by leveraging a set of “prior pose” models. On the contrary, we propose a bottom-up, data driven approach that directly predicts the 3D keypoint locations from local 2D features. We hypothesize

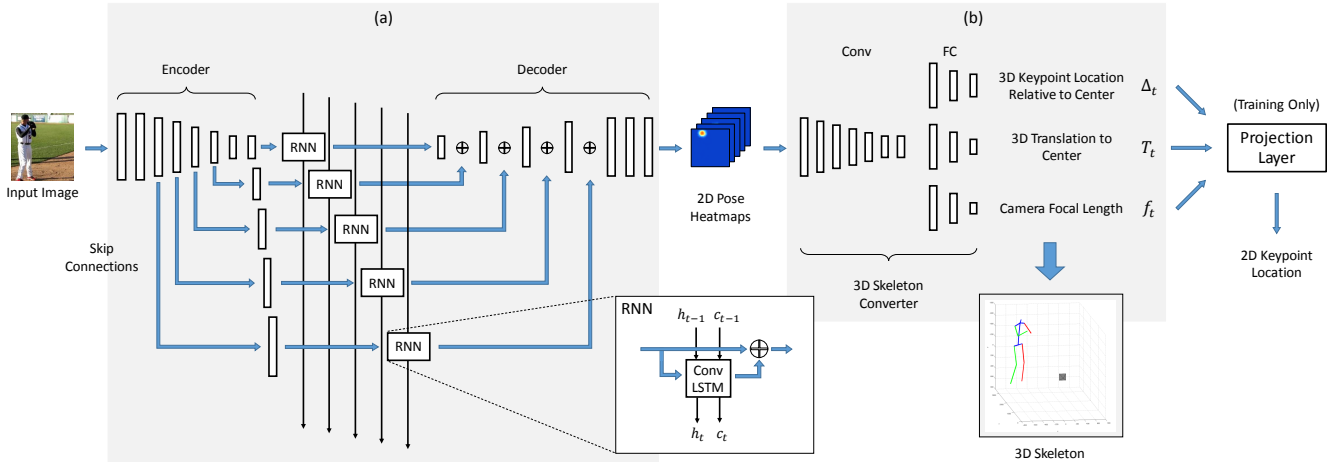


Figure 4: Architecture of the 3D-PFNet. (a) The recurrent hourglass architecture for 2D pose forecasting. (b) The 3D skeleton converter.

that the bottom-up reconstruction can outperform top-down approaches given sufficiently complex models and a vast amount of training data.

We model 3D skeletons and their 2D projection with a perspective projection model. Recall that a 3D skeleton $P \in \mathbb{R}^{3 \times N}$ is represented by N keypoints in the camera coordinate system. We can decompose P by $P = \Delta + T1^T$, where $\Delta \in \mathbb{R}^{3 \times N}$ represents the relative position of the N keypoints to their center in 3D, and $T \in \mathbb{R}^{3 \times 1}$ represents the translation to the center. Let f be the camera focal length and assume the principal point is at the image center. The goal of our 3D skeleton converter is to estimate $\{\Delta, T, f\}$ from the observed 2D heatmaps. Fig. 4 (b) details the architecture. The heatmaps generated at each timestep are first processed by another encoder. Now instead of connecting to a decoder, the encoder output is forwarded to three different branches. Each branch consists of three fully-connected layers, and the three branches will output Δ , T , and f , respectively. Note that estimating camera parameters is unnecessary if we have ground-truth 3D keypoint annotations to train our network. However, 3D pose data is hard to collect and thus are often unavailable in in-the-wild human pose datasets. With the estimated camera parameters, we can apply a projection layer [32] at the output of the network to project 3D keypoints to 2D, and measure the loss on reprojection error for training.

3.3. Training Strategy

Our 3D-PFNet is composed of multiple sub-networks. Different sub-networks serve different sub-tasks and thus can exploit different sources of training data. We therefore adopt a three-step, task-specific training strategy.

1) Hourglass The hourglass network (i.e. encoder and decoder) serves the task of single-frame 2D pose estimation. We therefore pre-train the hourglass network by lever-

aging large human pose datasets that provide 2D body joint annotations. We follow the training setup in [19] and apply a Mean Squared Error (MSE) loss for the predicted and ground-truth heatmaps.

2) 3D Skeleton Converter Training the 3D skeleton converter requires correspondences between 2D heatmaps and 3D ground truth of $\{\Delta, T, f\}$. We exploit the ground-truth 3D human poses from motion capture (MoCap) data. We synthesize training samples using a technique similar to [32]: First, we randomly sample a 3D pose and camera parameters (i.e. focal length, rotation, and translation). We then project the 3D keypoints to 2D coordinates using the sampled camera parameters, followed by constructing the corresponding heatmaps. This provides us with a training set that is diverse in both human poses and camera viewpoints. We apply an MSE loss for each output of Δ , T , and f , and an equal weighting to compute the total loss.

3) Full Network Finally, we train the full network (i.e. hourglass + RNNs + 3D skeleton converter) using static images and their corresponding pose sequences. To ease the training of LSTM, we apply curriculum learning similar to [34]: We start training the full network with pose sequences of length 2. Once the training converges, we increase the sequence length to 4 and resume the training. We repeat doubling the sequence length whenever training converges. We train the network with two sources of losses: The first source is the heatmap loss used for training the hourglass. Since we assume the 3D ground truths are unavailable in image and video datasets, we cannot apply loss directly on Δ , T , and f . We instead apply a projection layer as mentioned earlier and adopt an MSE loss on 2D keypoint locations. Note that replacing 3D loss with projection loss might diverge the training and output implausible 3D body poses, since a particular 2D pose can be mapped from multiple possible 3D configurations. We therefore initialize the

3D converter network with weights learned from the synthetic data, and keep the weights fixed during the training of the full network.

4. Experiments

We evaluate our 3D-PFNet on two tasks: (1) *2D pose forecasting* and (2) *3D pose recovery*.

4.1. 2D Pose Forecasting

Dataset We evaluate pose forecasting in 2D using the Penn Action dataset [39]. Penn Action contains 2326 video sequences (1258 for training and 1068 for test) covering 15 sports action categories. Each video frame is annotated with a human bounding box along with the locations and visibility of 13 body joints. Note that we do not evaluate our forecasted 3D poses due to the lack of 3D annotations in Penn Action. During training, we also leverage two other datasets: MPII Human Pose (MPII) [2] and Human3.6M [12]. MPII is a large-scale benchmark for single-frame human pose estimation. Human3.6M consists of videos of acting individuals captured in a controlled environment. Each frame is provided with the calibrated camera parameters and the 3D human pose acquired from MoCap devices.

Evaluation Protocol We preprocess Penn Action with two steps: First, since our focus is not on human detection, we crop each video frame to focus roughly around the human region: for each video sequence, we crop every frame using the tight box that bounds the human bounding box across all frames. Second, we do not assume the input image is always the starting frame of each video (i.e. we should be able to forecast poses not only from the beginning of a tennis forehand swing, but also from the middle or even shortly before the action finishes). Thus for a video with K frames, we generate K sequences by varying the starting frame. Besides, since adjacent frames contain similar poses, we skip frames when generating sequences. The number of frames skipped is video-dependent: Given a sampled starting frame, we always generate a sequence of length 16, where we skip every $(K - 1)/15$ frames in the raw video sequence after the sampled starting frame. This is to ensure that our forecasted output can “finish” each action in a predicted sequence of length 16. Note that once we surpass the end frame of a video, we will repeat the last frame collected until we obtain 16 frames. This is to force the forecasting to learn to “stop” and remain at the ending pose once an action has completed. Fig. 5 shows sample sequences of our processed Penn Action.

To evaluate the forecasted pose, we adopt the standard Percentage of Correct Keypoints (PCK) metric [2] from 2D pose estimation. PCK measures the accuracy of keypoint localization by considering a predicted keypoint correct if it falls within certain normalized distance of the ground truth.



Figure 5: Sample sequences of the processed Penn Action dataset. The action classes are: baseball swing, bench press, golf swing, jumping jacks, pull ups, and tennis serve.

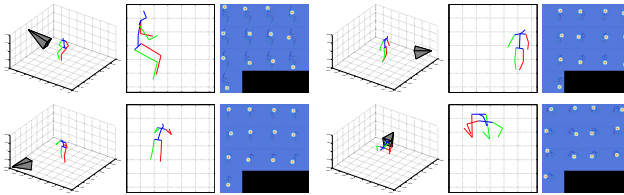


Figure 6: Samples of the synthetic data for training 3D skeleton converter. Each triplet consists of (1) the sampled 3D pose and camera in world coordinates, (2) the 2D projection, and (3) the converted heatmaps for 13 keypoints.

This distance is normalized typically based on the size of the full body bounding box [35] or the head bounding box [2]. Since we have already cropped the frames based on full body bounding boxes, we normalize the distance by $\max(h, w)$ pixels, where h and w are the height and width of the cropped image. We ignore invisible joints, and compute PCK separately for each of the 16 timesteps on the test sequences.

Implementation Details We use Torch7 [5] for our experiments. In all training, we use rmsprop for optimization. We train our 3D-PFNet in three steps as described in Sec. 3.3. First, we train the hourglass for single-frame pose estimation by pre-training on MPII and fine-tuning on the preprocessed Penn Action. For both datasets, we partition a subset of the training set for validation. Second, we train the 3D skeleton converter using Human3.6M. Note that the image data in Human3.6M are unused here, since we only need 3D pose data for synthesizing camera parameters and 2D heatmaps. Following the standard data split in [12], we use poses of 5 subjects (S1, S7, S8, S9, S11) for training and 2 subjects (S5, S6) for validation. Fig. 6 shows samples of our synthesized training data. We use mini-batches of size 64 and a learning rate of 0.001. Finally, we train the full 3D-PFNet on the preprocessed Penn Action. We apply the curriculum learning scheme until convergence at sequence length 16. At test time, we always generate pose sequences of length 16.

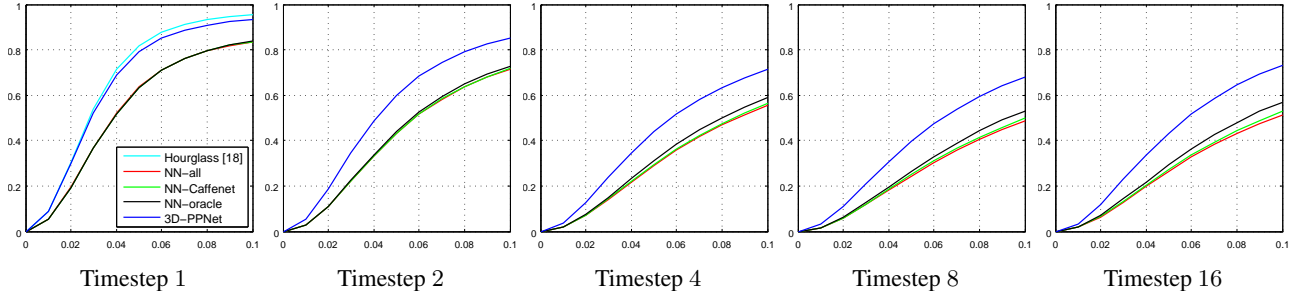


Figure 7: PCK curves at different timesteps. The x-axis is the distance threshold and the y-axis is the PCK value. The hourglass network [19] only estimates the current pose in timestep 1. Our 3D-PFNet outperforms all three NN baselines for all timesteps.

Timestep #	1	2	3	4	5	6	7	8	9	10	11	12	13	14	15	16
Hourglass [19]	81.9	-	-	-	-	-	-	-	-	-	-	-	-	-	-	-
NN-all	63.5	43.2	33.8	29.1	26.9	25.8	24.8	24.5	24.4	24.5	24.7	25.0	25.5	26.0	26.5	26.5
NN-CaffeNet	63.4	43.3	34.1	29.5	27.3	26.2	25.3	24.9	24.9	25.0	25.3	25.6	26.1	26.7	27.1	27.2
NN-oracle	63.4	44.1	35.5	31.2	29.1	28.0	27.0	26.5	26.5	26.8	27.3	27.6	28.1	28.8	29.2	29.3
3D-PFNet	79.2	60.0	49.0	43.9	41.5	40.3	39.8	39.7	40.1	40.5	41.1	41.6	42.3	42.9	43.2	43.3

Table 1: PCK values (%) with threshold 0.5 (PCK@0.05) for timestep 1 to 16.

Baselines Since there are no prior approaches for pose forecasting, we devise our own baselines for comparison. We consider three baselines based on *nearest neighbor* (NN). (1) *NN-all*: Given a test image, we first estimate the current human pose with an hourglass network and find the NN pose in the training images. We then transform the sequence of the NN pose to the test image as output. To measure distance between two poses (each represented by 13 2D keypoints), we first normalize the keypoints of each pose to have zero mean and unit maximum length from the center. We define distance by the MSE between two normalized poses. Since a ground-truth pose might contain invisible keypoints, we compute MSE only on the visible keypoints. Given the NN, we transform the associated sequence for the test image by reversing the normalization. (2) *NN-CaffeNet*: We hypothesize that the NN results can be improved by leveraging scene contexts. We therefore pre-filter the training set to keep only images with scene background similar to the test image before applying NN-all. We compute the Euclidean distance on the CaffeNet feature [13], and select the filtering threshold using a validation set. (3) *NN-oracle*: We exploit ground-truth action labels to keep only the training images with the same action category as the test image before applying NN-all. Note that this is a strong baseline since our method does not use ground-truth action labels.

Results Fig. 7 shows the PCK curves of our approach and the baselines at different timesteps (timestep 1 corresponds to the current frame). For all approaches, the PCK value decreases as timestep increases, since prediction becomes more challenging due to increasing ambiguity as we move further from the current observation. We also report the re-

sult of the hourglass network used for our 3D-PFNet. Since the hourglass network can only estimate the current pose, we only show its PCK curve in timestep 1. The three NN baselines achieve similar performance at timestep 1. As the timestep increases, NN-CaffeNet gradually outperforms NN-all, verifying our hypothesis that scene contexts can be used to reject irrelevant candidates and improve NN results. Similarly, NN-oracle gradually outperforms NN-CaffeNet, since the ground-truth action labels can improve the candidate set further. Finally, our 3D-PFNet outperforms all three baselines by significant margins. Fig. 8 shows qualitative examples of the poses forecasted by our 3D-PFNet.¹ Our 3D-PFNet can predict reasonable pose sequences in both 2D and 3D space. Fig. 9 shows failure cases of the NN baselines. The retrieved sequence of NN-all (top) is inconsistent with the context (i.e. a bowling alley) when the NN pose is from a different action class (i.e. baseball swing). By exploiting ground-truth action labels, NN-oracle (bottom) is able to retrieve a similar pose in the same context. However, the retrieved sequence still fails due to a small error in pose alignment, i.e. the person should be moving slightly toward the right rather than straight ahead. We believe the internal feature representation learned by our 3D-PFNet can better align human poses in the given context and thus can generate more accurate predictions. Tab. 3 reports the PCK with threshold 0.05 (PCK@0.05) for all 16 timesteps. Note that all PCK values stop decreasing after timestep 8. This is due to the subset of test sequences with repetitive ending frames, since prediction is easier for those cases as we only need to learn to stop and repeat the last predicted pose.

¹Also see <http://www.umich.edu/~ywchao/image-play/>.

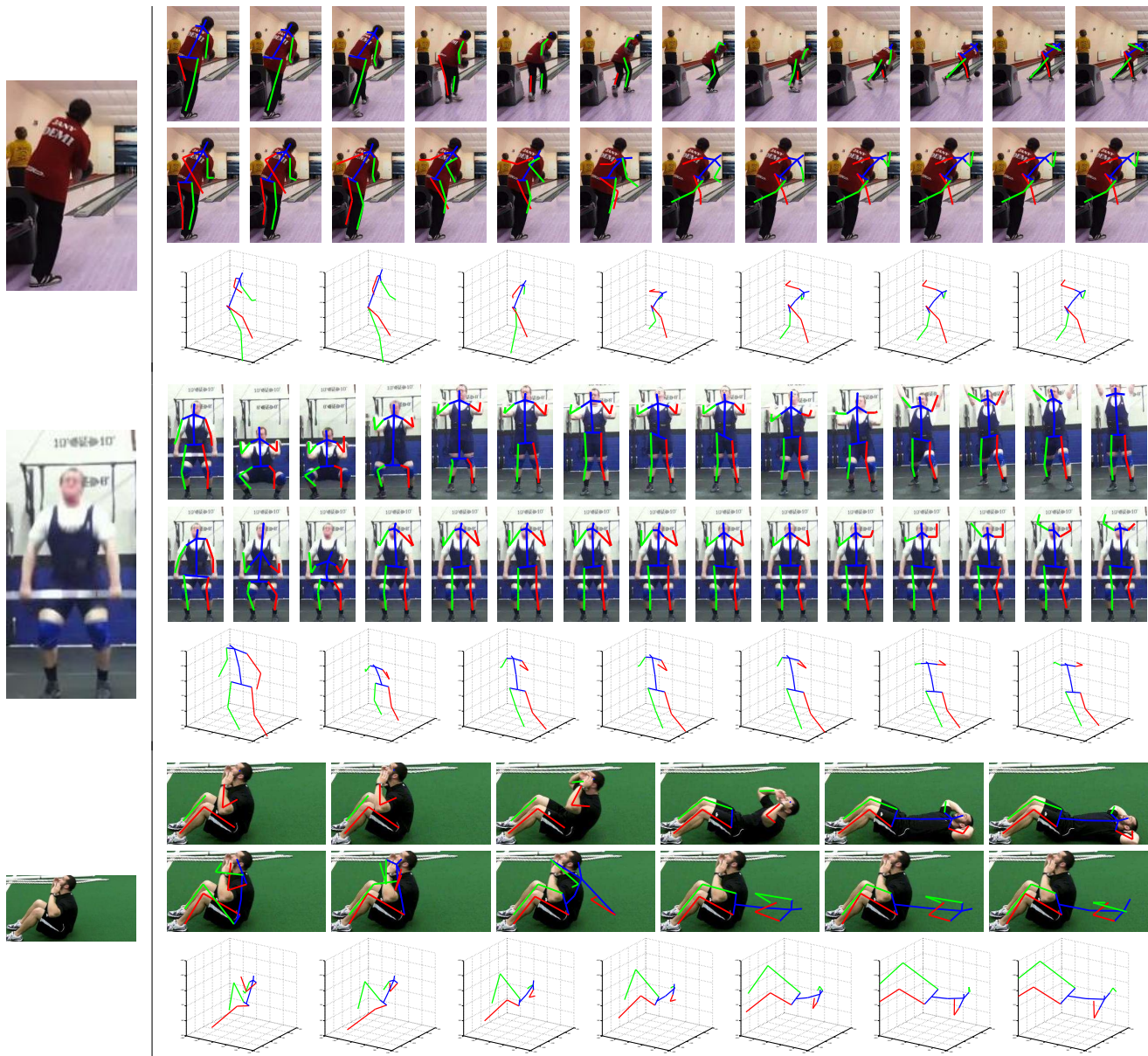


Figure 8: Qualitative results of pose forecasting. The left column shows the input images. For each input image, we show in the right column the sequence of ground-truth frame and pose (top) and our forecasted pose sequence in 2D (middle) and 3D (bottom). Note that some keypoints are not shown since they are labeled as invisible in the ground-truth poses.

4.2. 3D Pose Recovery

We separately evaluate the task of per-frame 3D skeleton recovery from 2D heatmaps on Human3.6M [12].

Setup We use the same data split as in training 3D-PFNet. However, we use video frames and generate heatmaps from hourglass rather than using synthetic data. For evaluation, we construct a validation set of 16150 images by sampling every 40 frames from all sequences and cameras of S5 and S6. Each frame is cropped with the tightest window that encloses the person bounding box while keeping the principal

point at image center. We evaluate the predicted 3D key-point positions relative to their center (i.e. Δ) with mean per joint position error (MPJPE) proposed in [12]. For training, we first fine-tune the hourglass on Human3.6M. We initialize the 3D skeleton converter with weights trained on synthetic data, and further train it with heatmaps from the hourglass.

Baselines We compare our 3D skeleton converter with two top-down approaches: the convex optimization based approach (Convex) proposed by Zhou *et al.* [40] and SM-

	Head	R.Sho	L.Sho	R.Elbow	L.Elbow	R.Wri	L.Wri	R.Hip	L.Hip	R.Knee	L.Knee	R.Ank	L.Ank	Avg
Convex [40]	145.3	123.5	122.8	139.1	129.5	162.2	153.0	115.2	111.8	172.1	171.7	257.4	258.5	158.6
SMPLify [3]	132.3	117.4	119.3	149.6	149.5	204.3	192.8	140.9	124.0	131.9	135.3	202.3	213.6	154.9
Ours	72.3	64.7	63.5	93.9	88.8	135.1	124.2	59.1	57.5	75.7	76.5	113.6	113.4	87.6

Table 2: Mean per joint position errors (mm) on Human3.6M. Our 3D converter achieves a lower error than the baselines on all joints.

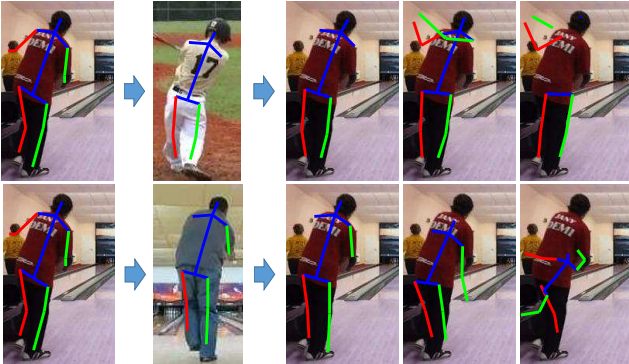


Figure 9: Failure cases of the NN baselines. Top: NN-all. Bottom: NN-oracle. Each row shows the input image with the estimated pose, the NN pose in the training set, and the transformed pose sequence of the NN pose on the input image.

PLify [3]. Since Convex assumes a weak perspective camera model, it can only estimate keypoint positions relative to their center up to a scaling factor. To generate poses with absolute scale, we first learn a prior on the length of human body limbs using the training data in Human3.6M, and scale their output pose to minimize the error between the predicted limb lengths and the prior. Besides, since Convex takes input of 2D keypoint coordinates rather than heatmaps, we sample 2D coordinates for each keypoint by searching for the maximum response in the heatmap. We also re-train the pose dictionary of Convex using the same training set of Human3.6M.

Results Tab. 2 shows the comparison of our approach against the baselines on 13 body joints. Our 3D skeleton converter achieves a lower error on all 13 body joints by a significant margin. The improvement over Convex is especially significant on the keypoints of knees and ankles (e.g. for left knee, from 171.7 to 76.5mm, and for left ankle, from 258.5 to 113.4mm). As pointed out in [32], Zhou *et al.*'s method assumes the input keypoint coordinates to be clean, which is not true for the hourglass output. Our approach, by training on heatmaps, can be adjusted to noisy input. Furthermore, our DNN-based, bottom-up approach, without using any pose priors, enjoys advantages over two top-down baselines, by learning to directly regress the 3D keypoint positions with a sufficiently complex model and a vast amount of training data. We show qualitative examples of our reconstructed 3D poses as well as the estimated camera poses in Fig. 10.

5. Conclusion

This paper presents the first study on forecasting human dynamics from static images. Our proposed 3D Pose Forecasting Network (3D-PFNet) integrates recent advances on single-image human pose estimation and sequence prediction, and further converts the 2D predictions into 3D space. We train the 3D-PFNet using a three-step training strategy to leverage a diverse source of training data, including image and video based human pose datasets and 3D Mo-Cap data. We demonstrate competitive performance of our 3D-PFNet on 2D pose forecasting and 3D pose recovery through quantitative and qualitative results.

References

- [1] I. Akhter and M. J. Black. Pose-conditioned joint angle limits for 3d human pose reconstruction. In *CVPR*, 2015. 2
- [2] M. Andriluka, L. Pishchulin, P. Gehler, and B. Schiele. 2d human pose estimation: New benchmark and state of the art analysis. In *CVPR*, 2014. 3, 5
- [3] F. Bogo, A. Kanazawa, C. Lassner, P. Gehler, J. Romero, and M. J. Black. Keep it smpl: Automatic estimation of 3d human pose and shape from a single image. In *ECCV*, 2016. 2, 8
- [4] W. Chen, H. Wang, Y. Li, H. Su, Z. Wang, C. Tu, D. Lischinski, D. Cohen-Or, and B. Chen. Synthesizing training images for boosting human 3d pose estimation. In *3DV*, 2016. 2, 10, 11
- [5] R. Collobert, K. Kavukcuoglu, and C. Farabet. Torch7: A matlab-like environment for machine learning. In *BigLearn, NIPS Workshop*, 2011. 5
- [6] J. Donahue, L. A. Hendricks, S. Guadarrama, M. Rohrbach, S. Venugopalan, T. Darrell, and K. Saenko. Long-term recurrent convolutional networks for visual recognition and description. In *CVPR*, 2015. 1
- [7] Y. Du, Y. Wong, Y. Liu, F. Han, Y. Gui, Z. Wang, M. Kankanhalli, and W. Geng. Marker-less 3d human motion capture with monocular image sequence and height-maps. In *ECCV*. 2016. 2
- [8] C. Finn, I. Goodfellow, and S. Levine. Unsupervised learning for physical interaction through video prediction. In *NIPS*. 2016. 2
- [9] K. Fragkiadaki, S. Levine, P. Felsen, and J. Malik. Recurrent network models for human dynamics. In *ICCV*, 2015. 1, 2
- [10] G. Gkioxari, A. Toshev, and N. Jaitly. Chained predictions using convolutional neural networks. In *ECCV*, 2016. 2
- [11] K. He, X. Zhang, S. Ren, and J. Sun. Deep residual learning for image recognition. In *CVPR*, 2016. 3

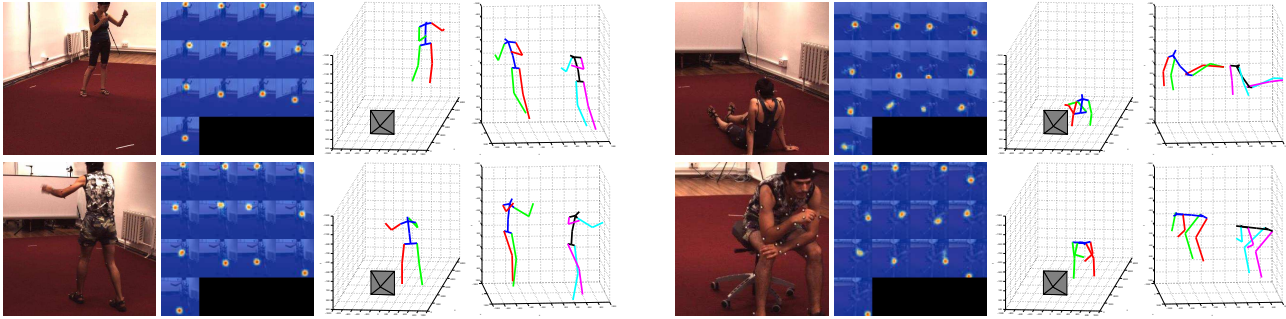


Figure 10: Qualitative results of 3D pose recovery. Each sample shows the input image, the heatmaps output of the hourglass, the estimated 3D pose and camera, and a side-by-side comparison with the ground-truth pose (colored by black, cyan, and magenta).

- [12] C. Ionescu, D. Papava, V. Olaru, and C. Sminchisescu. Human3.6m: Large scale datasets and predictive methods for 3d human sensing in natural environments. *TPAMI*, 36(7):1325–1339, July 2014. 5, 7
- [13] Y. Jia, E. Shelhamer, J. Donahue, S. Karayev, J. Long, R. Girshick, S. Guadarrama, and T. Darrell. Caffe: Convolutional architecture for fast feature embedding. *arXiv preprint arXiv:1408.5093*, 2014. 6
- [14] R. Jozefowicz, W. Zaremba, and I. Sutskever. An empirical exploration of recurrent network architectures. In *ICML*, 2015. 3
- [15] T. Lan, T.-C. Chen, and S. Savarese. A hierarchical representation for future action prediction. In *ECCV*, 2014. 2
- [16] S. Li and A. B. Chan. 3d human pose estimation from monocular images with deep convolutional neural network. In *ACCV*, 2014. 2
- [17] M. Mathieu, C. Couprie, and Y. LeCun. Deep multi scale video prediction beyond mean square error. In *ICLR*, 2016. 1, 2
- [18] R. Mottaghi, H. Bagherinezhad, M. Rastegari, and A. Farhadi. Newtonian image understanding: Unfolding the dynamics of objects in static image. In *CVPR*, 2016. 2
- [19] A. Newell, K. Yang, and J. Deng. Stacked hourglass networks for human pose estimation. In *ECCV*, 2016. 2, 3, 4, 6
- [20] B. X. Nie, C. Xiong, and S. C. Zhu. Joint action recognition and pose estimation from video. In *CVPR*, 2015. 2
- [21] S. L. Pinteá, J. C. van Gemert, and A. W. M. Smeulders. Déjà vu: Motion prediction in static images. In *ECCV*, 2014. 1, 2
- [22] G. Rogez and C. Schmid. Mocap-guided data augmentation for 3d pose estimation in the wild. In *NIPS*. 2016. 2
- [23] Z. Shou, D. Wang, and S.-F. Chang. Temporal action localization in untrimmed videos via multi-stage cnns. In *CVPR*. 2016. 1
- [24] K. Simonyan and A. Zisserman. Two-stream convolutional networks for action recognition in videos. In *NIPS*. 2014. 1
- [25] N. Srivastava, E. Mansimov, and R. Salakhutdinov. Unsupervised learning of video representations using lstms. In *ICML*, 2015. 1, 2
- [26] B. Tekin, I. Katircioglu, M. Salzmann, V. Lepetit, and P. Fua. Structured prediction of 3d human pose with deep neural networks. In *BMVC*, 2016. 2
- [27] J. J. Tompson, A. Jain, Y. LeCun, and C. Bregler. Joint training of a convolutional network and a graphical model for human pose estimation. In *NIPS*. 2014. 2
- [28] C. Vondrick, H. Pirsiavash, and A. Torralba. Generating videos with scene dynamics. In *NIPS*. 2016. 2, 3
- [29] J. Walker, C. Doersch, A. Gupta, and M. Hebert. An uncertain future: Forecasting from static images using variational autoencoders. In *ECCV*, 2016. 1, 2, 3
- [30] J. Walker, A. Gupta, and M. Hebert. Patch to the future: Unsupervised visual prediction. In *CVPR*, 2014. 1, 2
- [31] J. Walker, A. Gupta, and M. Hebert. Dense optical flow prediction from a static image. In *ICCV*, 2015. 1, 2
- [32] J. Wu, T. Xue, J. J. Lim, Y. Tian, J. B. Tenenbaum, A. Torralba, and W. T. Freeman. Single image 3d interpreter network. In *ECCV*, 2016. 2, 3, 4, 8
- [33] T. Xue, J. Wu, K. L. Bouman, and W. T. Freeman. Visual dynamics: Probabilistic future frame synthesis via cross convolutional networks. In *NIPS*. 2016. 2
- [34] J. Yang, S. E. Reed, M.-H. Yang, and H. Lee. Weakly-supervised disentangling with recurrent transformations for 3d view synthesis. In *NIPS*. 2015. 4
- [35] Y. Yang and D. Ramanan. Articulated human detection with flexible mixtures of parts. *TPAMI*, 35(12):2878–2890, Dec 2013. 5
- [36] H. Yasin, U. Iqbal, B. Krüger, A. Weber, , and J. Gall. A dual-source approach for 3d pose estimation from a single image. In *CVPR*, 2016. 2
- [37] S. Yeung, O. Russakovsky, G. Mori, and L. Fei-Fei. End-to-end learning of action detection from frame glimpses in videos. In *CVPR*. 2016. 1
- [38] J. Yuen and A. Torralba. A data-driven approach for event prediction. In *ECCV*, 2010. 1, 2
- [39] W. Zhang, M. Zhu, and K. G. Derpanis. From actemes to action: A strongly-supervised representation for detailed action understanding. In *ICCV*, 2013. 5
- [40] X. Zhou, S. Leonardos, X. Hu, and K. Daniilidis. 3d shape estimation from 2d landmarks: A convex relaxation approach. In *CVPR*, 2015. 2, 3, 8
- [41] X. Zhou, M. Zhu, S. Leonardos, K. G. Derpanis, and K. Daniilidis. Sparseness meets deepness: 3d human pose estimation from monocular video. In *CVPR*, 2016. 2

Timestep #	1	2	3	4	5	6	7	8	9	10	11	12	13	14	15	16	# Tr
Baseball pitch	79.7	51.2	37.4	30.3	26.3	23.6	22.2	21.5	20.8	20.6	20.5	20.7	20.8	20.7	20.6	20.5	94
Baseball swing	81.2	69.0	54.9	46.7	42.3	40.2	39.1	38.7	38.8	38.9	38.7	38.9	39.0	38.8	38.8	38.7	104
Bench press	69.1	60.6	52.6	50.1	48.8	48.7	48.9	49.3	49.9	50.5	51.3	52.1	52.9	53.6	54.1	54.3	63
Bowl	68.8	53.1	41.1	34.9	31.7	30.0	28.9	28.4	27.7	27.3	27.0	26.9	26.9	27.0	26.9	27.0	123
Clean and jerk	87.5	60.1	52.7	47.9	44.6	41.6	39.9	38.5	38.0	37.5	37.1	36.8	36.9	37.0	37.1	37.1	39
Golf swing	82.1	68.7	59.4	54.2	51.6	50.3	49.8	49.3	48.6	47.5	47.3	47.6	48.0	48.0	47.8	47.6	81
Jump rope	83.6	69.4	60.6	61.1	65.4	69.2	65.6	61.9	62.2	64.9	66.1	64.6	64.2	65.6	67.2	67.6	36
Jumping jacks	85.0	63.9	47.1	41.3	40.7	42.9	46.7	50.0	52.6	53.9	55.4	57.9	60.5	62.9	64.9	65.5	51
Pullup	81.4	65.7	50.9	44.3	42.1	42.3	43.4	44.8	46.7	48.8	50.8	52.5	54.4	55.7	56.4	56.5	89
Pushup	73.3	65.5	57.5	53.1	51.4	51.3	51.9	53.2	54.9	56.6	58.4	60.1	61.6	62.7	63.2	63.2	94
Situp	67.1	48.0	41.6	38.9	37.6	37.1	37.4	38.0	39.0	39.6	40.4	41.2	41.8	42.3	42.6	42.8	45
Squat	81.3	58.4	46.1	42.3	40.8	41.1	42.3	43.7	45.5	47.4	49.3	51.2	53.0	54.8	56.0	56.0	104
Strum guitar	62.4	61.6	61.5	61.2	61.1	61.6	61.1	60.7	60.3	60.2	59.7	59.2	58.6	58.5	58.4	58.3	42
Tennis forehand	80.9	59.3	40.8	31.7	27.4	24.7	22.9	22.0	21.0	20.5	20.1	19.9	19.8	19.7	19.7	19.6	73
Tennis serve	78.8	56.4	41.3	34.1	29.5	26.4	24.3	22.8	21.6	20.7	20.3	20.0	20.0	20.3	20.3	20.2	104

Table 3: PCK@0.05 of 3D-PFNet on individual action classes.

A. Supplementary Material

<http://www.umich.edu/~ywchao/image-play/>.

A.1. Human Character Rendering

We demonstrate one potential application of 3D pose forecasting by rendering human characters from 3D skeletal poses. We use the public code provided by Chen *et al.* [4]: We first produce a 3D human shape model from each 3D skeletal pose using SCAPE. We then transfer skin and clothing textures to the 3D human model. Finally, the 3D model is rendered and overlaid on the person’s projected bounding box in the input image. Fig. 11 shows the rendered human characters, both textureless and textured, for the qualitative results shown in the Fig. 8 of the paper. We believe the capability of pose forecasting with 3D human rendering may trigger further applications in augmented reality.

A.2. Performance on Individual Action Classes

Tab. 3 shows the PCK and the number of training videos of each action class. We see that actions with holistic joint motions (e.g. baseball pitch) are more challenging for pose forecasting and thus have lower PCK values even with more training samples, while actions with only partial joint motions (e.g. jump rope) are the opposite.

A.3. Additional Qualitative Results

We show additional qualitative examples of the forecasted poses in Fig. 12, 13, and 14. Note that the rendered human model also improves the interpretability of the output 3D poses over skeletons. The second example in Fig. 14 shows a failure case of 3D pose recovery. While the forecasted motion of the tennis serve looks plausible in 2D (row 2), the recovered 3D poses are unrealistic in their body configurations (row 4 and 5), which may be difficult to perceive in the visualizations of 3D skeletons (row 3). All qualitative results can also be viewed as videos at

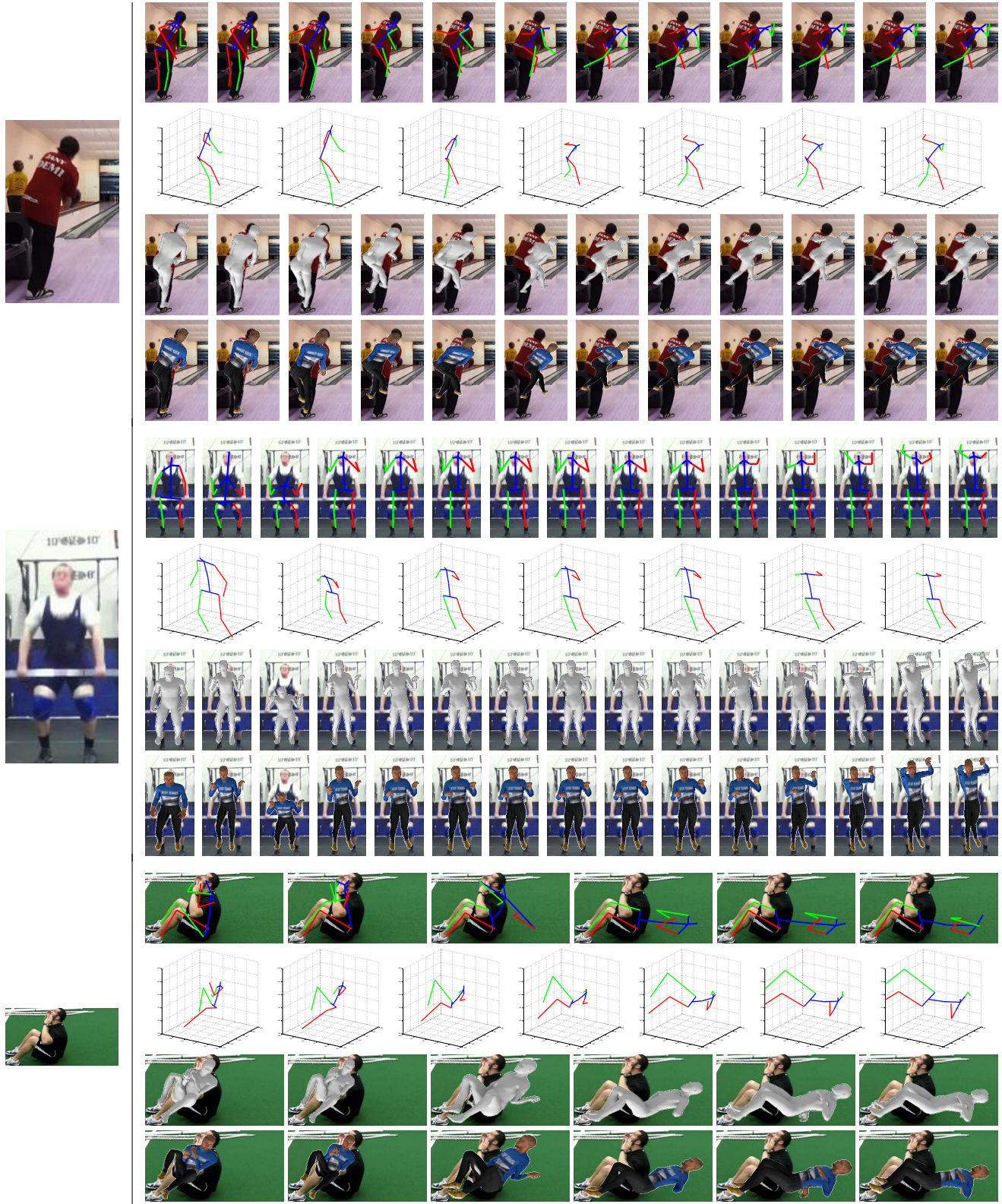


Figure 11: Rendering human characters from the forecasted 3D skeletons. The left column shows the input images. For each input image, we show in the right column our forecasted pose sequence in 2D (row 1) and 3D (row 2), and the rendered human body without texture (row 3) and with skin and cloth textures (row 4). We use the rendering code provided by [4].

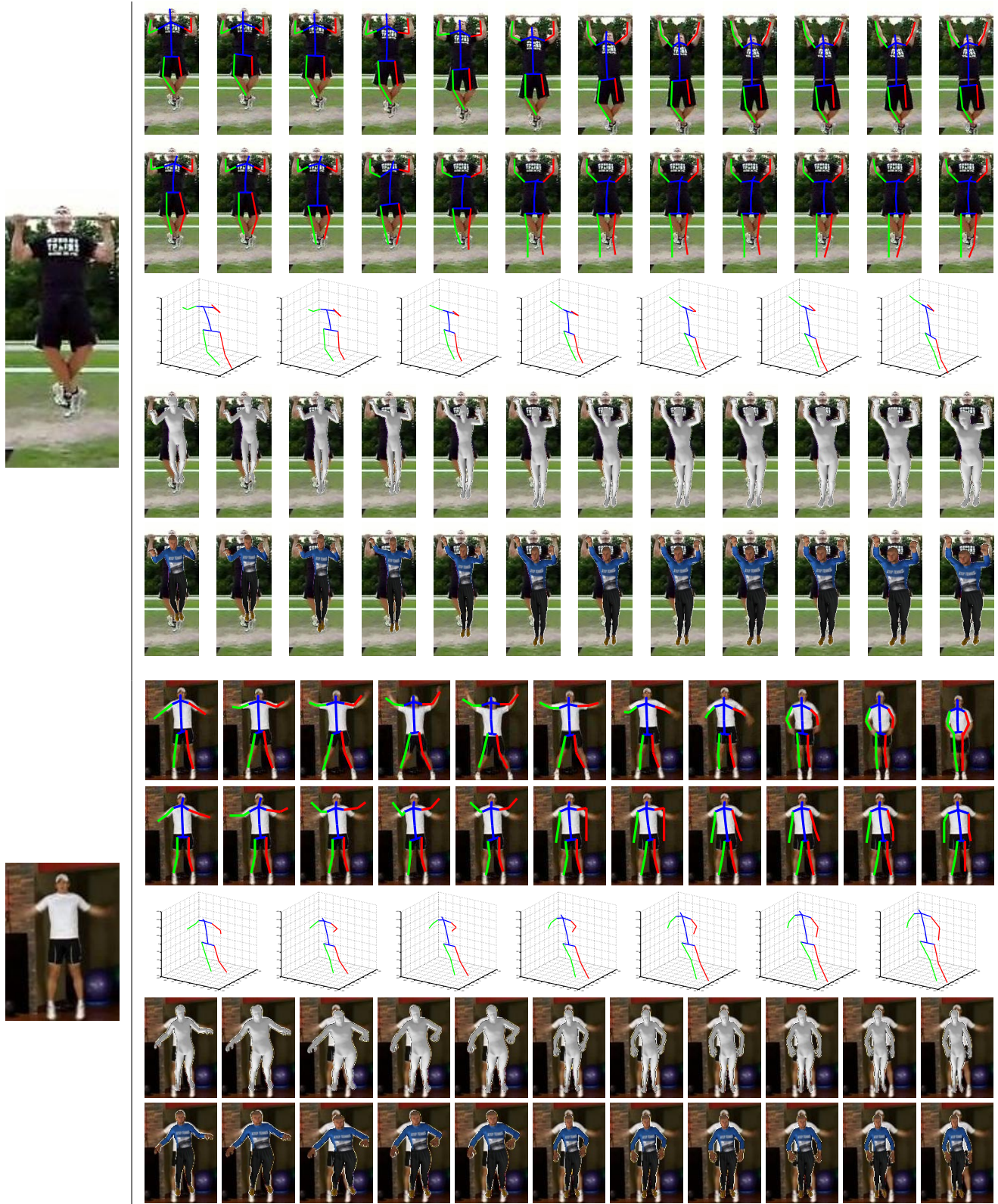


Figure 12: Additional qualitative results of pose forecasting. The left column shows the input images. For each input image, we show in the right column the sequence of ground-truth frame and pose (row 1), our forecasted pose sequence in 2D (row 2) and 3D (row 3), and the rendered human body without texture (row 4) and with skin and cloth textures (row 5).

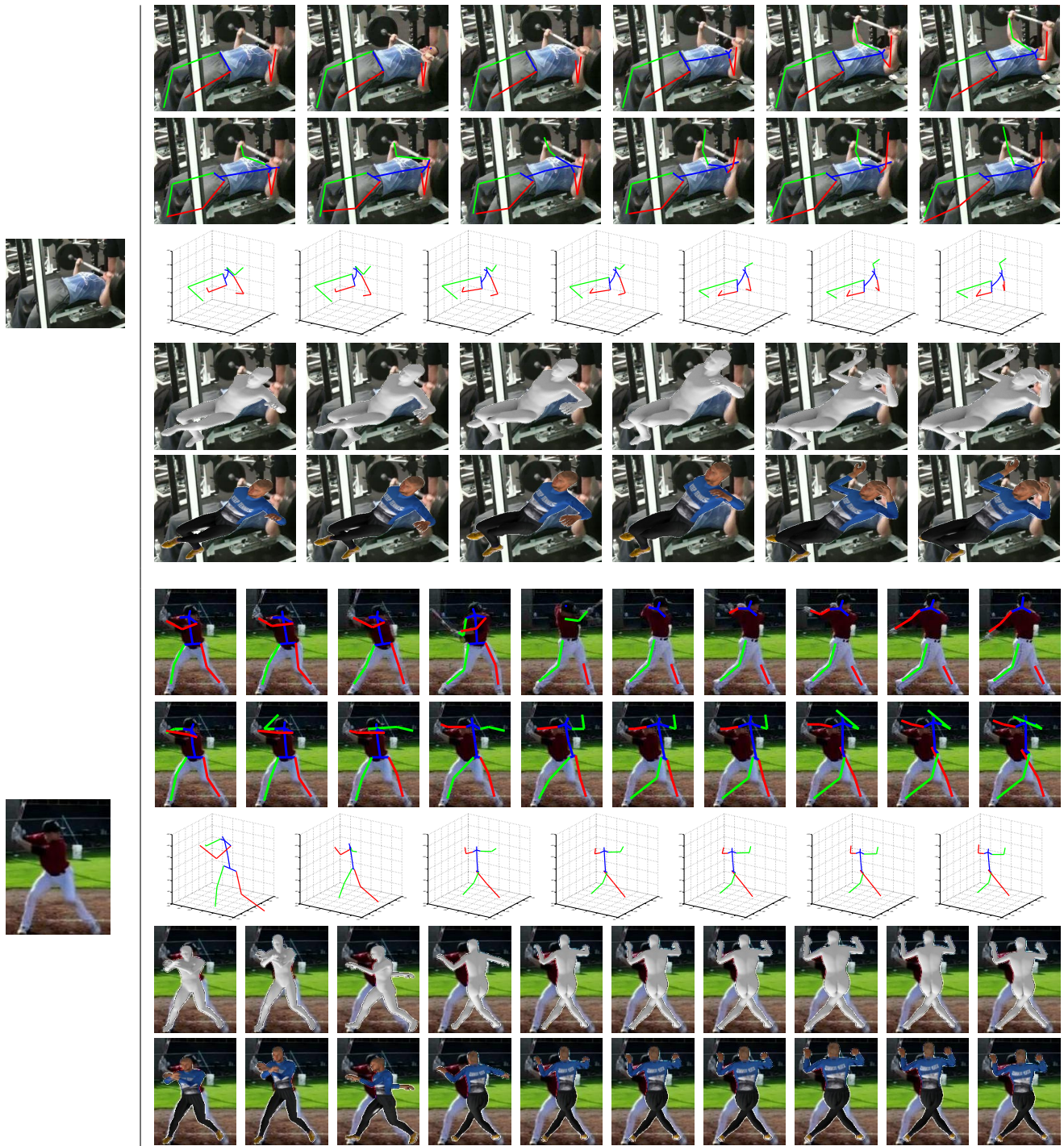


Figure 13: Additional qualitative results of pose forecasting. The left column shows the input images. For each input image, we show in the right column the sequence of ground-truth frame and pose (row 1), our forecasted pose sequence in 2D (row 2) and 3D (row 3), and the rendered human body without texture (row 4) and with skin and cloth textures (row 5).

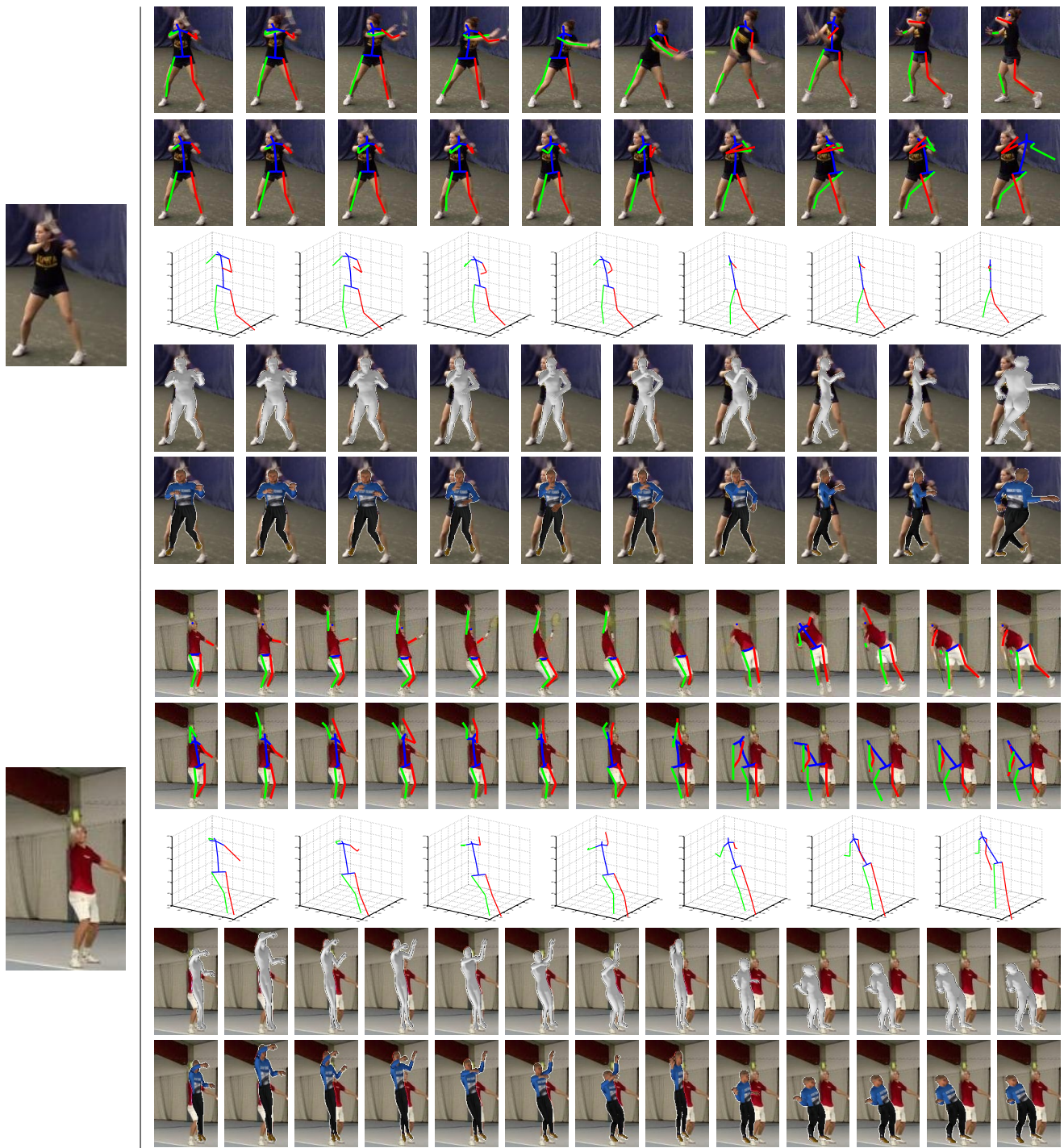


Figure 14: Additional qualitative results of pose forecasting. The left column shows the input images. For each input image, we show in the right column the sequence of ground-truth frame and pose (row 1), our forecasted pose sequence in 2D (row 2) and 3D (row 3), and the rendered human body without texture (row 4) and with skin and cloth textures (row 5).